Eng Int Syst (2022) 5: 341–351

Engineering
Intelligent Systems

A Target Detection Algorithm of Aerial Images in Power Grid Inspection Based on Transfer Learning

Feng Wang[1,*], Li Shen[1] and Wen Li[2]

[1] *Center of Research, Zhejiang Huayun Information Technology Co., Ltd., Hangzhou 310012, China*
[2] *Center of Information, Guodian Zhejiang Beilun First Power Generation Co., Ltd., Ningbo 315800, China*

When the traditional algorithm is applied to detect a target in aerial images during power grid inspection, it is difficult to carry out optical correction due to the great influence of the noise of aerial images. In the target coincidence rate range of 29.56%–49.56% of aerial images, there is the problem of high recall rate. Therefore, this paper proposes a target detection algorithm for aerial images in power grid inspection based on transfer learning. First of all, the aerial images are preprocessed, which involves optical correction, image restoration, geometric correction and so on. Then the SIFT algorithm based on the Gaussian scale space theory is used to extract the target feature points of the aerial images. The main implementation process involves: establishing the boundaries of the scale space, the feature point location, the feature point orientation, and the feature point descriptor generation. Based on the transfer learning algorithm, the detection of targets in aerial images in power grid inspection is realized, and the target detection algorithm is completed. In order to prove that the algorithm has a low recall rate in the range of 29.56%–49.56% of the target coincidence rate of the aerial images in power grid inspection, compared with the original algorithm, the experimental results show that the recall rate of the algorithm is always lower than that of the other two algorithms, and the performance is better.

Keywords: transfer learning, aerial images in power grid inspection, target detection algorithm, optical correction

1. INTRODUCTION

The target detection algorithm of the aerial images in power grid inspection can identify and locate the insulator, bird's nest and other targets on the tower. The power system is the lifeblood of the country; hence, the transmission line is an essential part of this system, and the normal and efficient operation of the transmission line is an important guarantee for the stable development of the national economy. With the development of electric power systems in China, the distance between transmission lines is increasing, and the transmission lines are being installed further away from the city and the main roads. Generally, traditional inspection and maintenance of transmission lines is done manually, with the main detection method being the naked eye or binoculars for observation. When the problem cannot be detected in this way, it is necessary to climb the tower to check lines one by one, which is time consuming and inadequate given the current domestic and industrial needs (Zhang et al., 2018; Gian et al., 2019). With the development of power technology, optical technology, aviation technology and image processing technology, the use of aerial images for line inspection has become the future development direction. Using helicopter and UAV to inspect the transmission line has the advantages of

---

**Corresponding Author Email: wangfenghz1@163.com

reliability, rapidity, low cost and not limited to the surrounding environment. By storing, processing and analyzing the inspection images, a lot of information about the operation of transmission lines can be obtained. The information can give a comprehensive understanding of the condition of transmission lines and provides data for the inspection of the transmission line. At present, the inspection of transmission lines based on aerial photos mainly uses manual methods to detect any problems. Due to the uncertainty of visual observation, it is easy to miss and misjudge the line defects (Hou et al., 2018). In addition, the amount of data collected by aerial photography is very large, and its inspection requires a lot of manpower and material resources. Hence, a target detection algorithm for aerial images in power grid inspection is emerging at an appropriate time (Dániello et al., 2018).

For the target detection algorithm of aerial images in power grid inspection, some preliminary research results have been obtained by researchers at home and abroad. Foreign scholars have proposed a target detection algorithm which uses a ratio operator to extract the pixel points of aerial images, a subsection Radon transform to extract and connect each section of the transmission line, and then a Kalman filter technology to track the broken part of the connected transmission line, in order to remove the damaged line . Finally, the ratio operator is used to detect the target on the transmission line (Wang et al., 2018; Chowdhary and Kumar, 2019). However, the research on the detection algorithm of the aerial images in power grid inspection is still in its infancy in our country. Image processing technology for aerial images in power grid inspection does not have a long application history, the research results are few and mainly relate to the stability of image acquisition and the improvement of image quality, and there is still little research on the detection of targets in the aerial images in power grid inspection. However, some scholars have put forward some constructive opinions and methods. Some scholars have put forward a target detection algorithm based on genetic algorithm. Firstly, neural network is used to filter out the background noise of aerial images in power grid inspection, then the image is segmented by the method of maximum entropy threshold in genetic algorithm, and finally the aerial images in power grid inspection is segmented by the method of connected region (Nagaraj et al., 2018). These methods preliminarily solve the problem of target detection of aerial images in power grid inspection. However, in the process of using the above algorithm to detect the target of aerial images in power grid inspection, it is unable to carry out optical correction due to the great influence of aerial image noises in power grid inspection. In the range of 29.56%–49.56% of target coincidence rate of aerial images in power grid inspection, there is a high recall rate problem. Therefore, a target detection algorithm of aerial images in power grid inspection based on transfer learning is proposed.

2. DESIGN OF TARGET DETECTION ALGORITHM OF AERIAL IMAGES IN POWER GRID INSPECTION BASED ON TRANSFER LEARNING

2.1 Image Preprocessing

First of all, the inspection image of power aerial photography is preprocessed, which includes optical correction, image restoration, geometric correction and so on. The purpose of image restoration is to remove the noise and motion blur in the aerial images in power grid inspection, and highlight the useful information in the image. The purpose of optical correction is to solve the exposure and focus problems when taking aerial photographs and improve the image contrast. The geometric correction (distortion restoration) process corrects the geometric deformation of the aerial image, and carries out several operations on the image (Luo et al., 2018).

2.1.1 Optical Correction of Aerial Images in Power Grid Inspection

The optical correction of aerial images in power grid inspection needs nonlinear transformation first, and then histogram equalization (He et al., 2018).

If f is the gray level of the image and L is the incident light intensity of the CCD image sensor, the relationship between the input light intensity and the gray level of the image can be expressed as follows:

$$f = cL^{\gamma} \tag{1}$$

In Equation (1), c represents constant; γ represents input light intensity.

According to Equation (1), the gray level of the image has a nonlinear relationship with the input light intensity. In order to correct this and make it linear, it must be transformed.

$$g = kL\left(\frac{f}{c}\right)^{\frac{1}{\gamma}} \tag{2}$$

In Equation (2), g, represents the gray level of the transformed image; k, represents the constant, usually 1.

In Equation (2), different values of γ have different effects after transformation. When $\gamma < 1$, the brighter the input value, the stronger is the output value; that is, the image becomes brighter. When $\gamma > 1$, the brighter the input value, the weaker is the output value; that is, the image becomes darker. When $\gamma = 1$, it is expressed as linear transformation, and the image brightness remains unchanged. Therefore, the value of γ is directly related to the effect of image transformation (Maria, 2018; Gao and Gu, 2018). The value of γ is selected by the gray level feature of the image.

Set a gray-scale image with a resolution of $m \times n$, $\overline{g}$, is its average gray-scale feature, and its calculation equation is as follows:

Table 1 Corresponding relationship between average gray $\overline{g}$ and γ value.

No.	Average Gray $\overline{g}$	γ value
1	200–210	1.6
2	190–200	1.4
3	180–190	1.2
4	170–180	1
5	150–170	0.8
6	130–150	0.7
7	110–130	0.6
8	90–110	0.5

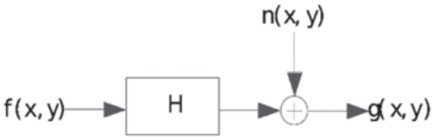

Figure 1 Degradation model.

$$\overline{g} = \frac{1}{m \times n} \sum_{i=1}^{n} \sum_{j=1}^{m} f(i, j) \tag{3}$$

In Equation (3), $f(i, j)$ represents the gray value on point (i, j).

Using the average gray $\overline{g}$ to represent the gray characteristics of the gray image, the corresponding relationship between the average gray $\overline{g}$ and the γ value is shown in Table 1. The value of γ is selected according to Table 1 (Lou et al., 2018).

Then, through histogram equalization, the uneven histogram distribution of aerial images in power grid inspection is transformed so that it has uniform distribution, and the dynamic range of gray value is increased to enhance the overall contrast of the image. Firstly, the following method is used to process the aerial images:

$$g(i, j) = T[f(i, j)] \tag{4}$$

In Equation (3), $g(i, j)$ represents the image after enhancement processing; T represents the image enhancement transformation function, that is, an operation on the original image, which is defined in the neighborhood of (i, j).

If s and t represent the gray value of the original image and the image after enhancement on point (i, j) respectively, the processing can be expressed as follows:

$$t = T(s) \tag{5}$$

At this time, the image enhancement transform function T needs to meet two conditions:

1) $T(s)$ is a single valued single increasing function in the range of $0 \leq s \leq L - 1$;

2) For $0 \leq s \leq L - 1$, there is $0 \leq T(s) \leq L - 1$.

Condition 1) ensures the existence of inverse transformation, and the sequence of gray levels of the source image remains from small to large after transformation, so as to prevent the reversed gray level of the transformed image. Condition 2) ensures the consistency of the dynamic range of gray levels before and after transformation. In histogram equalization, the cumulative distribution function needs to meet these two conditions, and can convert the distribution of s into the uniform distribution of t (Pavela, 2018). At this time, the cumulative distribution function CDF of s is the cumulative histogram of the original image. In this case, the equation is:

$$t_k = T(s_k) \tag{6}$$

In Equation (6), k represents the gray level of the digital image.

At this time, the value of t_k is within [0, 1], and it needs to be extended to $[0, L - 1]$ and integer.

Then the equation for calculating the gray level of the output image is:

$$y_k = \mathrm{int}[(L - 1)t_k + 0.5] \tag{7}$$

In Equation (7), y_k represents the gray level of the output image.

2.1.2 Restoration of Aerial Images in Power Grid Inspection

Image restoration is done by processing the degraded image and restoring the original image as much as possible. The key to restoring aerial images in power grid inspection is to establish the degradation model of the aerial images. Because there are many reasons for image degradation, only an approximate model can be built to describe the degradation of the image (Jonsson, 2018).

Assuming that the real image on the object plane is represented by $f(x, y)$, and the influence of external additive noise $n(x, y)$ is introduced into an imaging system H at the same time, the actual degraded image $g(x, y)$ can be described by the degradation model, as shown in Figure 1.

Expressed mathematically, the input and output in Figure 1 have the following forms:

$$g(x, y) = H[f(x, y)] + n(x, y) \tag{8}$$

In Equation (8), $H[\cdot]$ represents the transformation function considering all degradation factors. It has the following properties: homogeneity, superposition, linearity and space invariance. It can be used as a linear operator (Jiang et al., 2018).

According to the linear system theory, there are:

$$\begin{aligned} H[f(x,y)] &= H[f(x,y) * \delta(x,y)] \\ &= f(x,y) * H[\delta(x,y)] \\ &= f(x,y) * h(x,y) \end{aligned} \tag{9}$$

In Equation (9), $\delta(x, y)$ is the unit impulse signal; $h(x, y)$ is the transformation function of the unit impulse signal.

Without considering the additive noise, the response of the degradation model is as follows:

$$\begin{aligned} g(x,y) &= H[f(x,y)] = f(x,y) * h(x,y) \\ &= \iint\limits_{R^2} f(\alpha,\beta)h(x-\alpha, y-\beta)d\alpha d\beta \end{aligned} \tag{10}$$

In Equation (10), R represents degradation threshold; α and β represent linear response value and linear degradation value respectively; d represents response threshold.

Because $H[\cdot]$ is space invariant, the response of the model to the displacement signal $f(x - x_0, y - y_0)$ is:

$$f(x-x_0, y-y_0) * h(x,y) = g(x-x_0, y-y_0) \tag{11}$$

In Equation (11), $g(x - x_0, y - y_0)$ represents degraded signal.

In the case of additive noise, the above degradation model can be expressed as:

$$g(x,y) = f(x,y) * h(x,y) + n(x,y) \tag{12}$$

Through the degradation model of the aerial images in power grid inspection, the degraded image of the aerial images in power grid inspection is processed, and the original source image is restored (Hou et al., 2018).

2.1.3 Geometric Correction of Aerial Images in Power Grid Inspection

The geometric correction algorithm based on the iterative method and self-checking polynomial compensation error is used to carry out the geometric correction of aerial images in power grid inspection. This involves the following steps:

In the first step, according to the ephemeris attitude data provided by the satellite system, Lagrange function and linear function are used to fit the external azimuth elements to obtain the initial value G_0; Then, based on the set of control points, G_0 is adjusted to obtain the external azimuth element G, and the strong correlation between the external azimuth elements is overcome by using the generalized ridge estimation method (Liu et al., 2018).

In the second step, the exterior orientation elements of each scanned line are accurately obtained by the cyclic iteration method, and then the image plane coordinates of the ground points are obtained according to the collinear equation model, which is the initial coordinate estimation of geometric correction processing.

The third step is to check the discrepancy between the estimated value of image plane coordinate and the real value at the control point, construct the self-checking polynomial with the estimation deviation and carry out the least square fitting. Using the above fitting coefficient, the error compensation of the initial coordinate estimated value obtained in step 2 is realized to traverse each point in the image and carry out the gray-scale interpolation.

2.2 Extraction of Target Feature Point

The SIFT algorithm based on the Gaussian scale space theory is used to extract the target feature points of the aerial images in power grid inspection. The main implementation process involves obtaining the extreme value of the scale space, the feature point location, the feature point orientation, and generating the feature point descriptor.

2.2.1 Extreme Value of Scale Space

In order to give the detected feature points scale attributes, it is necessary to establish the scale space of the aerial image in the power grid inspection (Zou et al., 2018). The scale space $L(x, y, \sigma)$ of image $I(x, y)$ is obtained by convolution of a series of Gaussian check images:

$$L(x,y,\sigma) = G(x,y,\sigma) * I(x,y) \tag{13}$$

In Equation (13), $G(x, y, \sigma)$ represents Gaussian kernel function and σ represents the standard deviation of the Gaussian smoothing filter.

In order to effectively detect the stable feature points in the scale space, the Gaussian difference function DOG of the image is constructed as the approximation of the normalized Gaussian Laplace function $\sigma^2\nabla^2 G$, which can be calculated by the following equation:

$$\begin{aligned} D(x,y,\sigma) &= (G(x,y,k\sigma_I) - G(x,y,\sigma_I)) * I(x,y) \\ &= L(x,y,k\sigma_I) - L(x,y,\sigma_I) \end{aligned} \tag{14}$$

In Equation (14), $D(x, y, \sigma)$ represents the Gaussian difference function of image; k represents the scale ratio between adjacent scale images; σ_I represents the standard deviation of Gaussian smoothing filter of image I (Milliat and Agnès, 2018).

Because the local extremum of Gauss difference function is scale invariant, the scale invariant characteristic point X of its scale space can be defined as:

$$X = (x,y,\sigma)^T = extrema\{D(x,y,\sigma)\} \tag{15}$$

In Equation (15), T represents the scale threshold; *extrema* represents the local extreme point in the $3 \times 3 \times 3$ neighborhood of the function DOG, as shown in Figure 2.

2.2.2 Feature Point Location

Because the DOG operator is sensitive to noise and edge, it is necessary to further test the candidate feature points to locate them accurately. The exact location and scale of the feature points are determined by the following operations, and the low contrast (sensitive to noise) and unstable edge response points are removed.

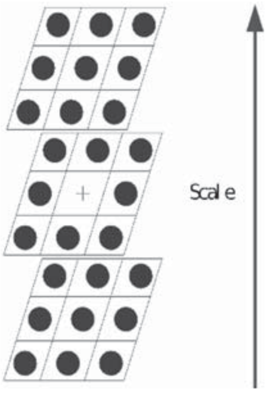

Figure 2 Local extremum in 3 × 3 × 3 neighborhood of function DOG.

Taylor quadratic expansion of Gauss difference function is carried out at the extreme value:

$$D(X) = D + \frac{\partial D^T}{\partial X}\Delta X + \frac{1}{2}\Delta X^T \frac{\partial^2 D}{\partial X^2}\Delta X \tag{16}$$

In Equation (16), $D(X)$ represents the Taylor quadratic expansion result at the extreme value of Gauss difference function; D represents the threshold value of DOG operator; ΔX represents the offset of sample point (Sophie, 2018).

Since X is the extreme point of Gauss difference function, the following equation holds:

$$\frac{\partial D(X)}{\partial X} = 0 \tag{17}$$

The migration can be obtained by solving the equation

$$\Delta X = -\frac{\partial D}{\partial X}\left(\frac{\partial^2 D}{\partial X^2}\right)^{-1} \tag{18}$$

If the offset of X in any dimension is less than 0.5, the extreme point is confirmed as the feature point; if ΔX is greater than 0.5, it means that the position of the current point has been shifted to the adjacent point, and the position of the current point needs to be repeatedly corrected until the offset is less than 0.5. The function value $D(\overline{X})$ can be obtained by substituting the modified result $\overline{X}$ into Equation (16), and the unstable extreme points of low contrast can be filtered according to this value. The contrast threshold is set to T_c, and finally all the low contrast points of $D(\overline{X}) < T_c$ are removed.

Because of the strong edge response of the DOG function, in order to obtain stable feature points, it is necessary to remove the points with a high edge response. For the peak value with poor accuracy in the function DOG, the main curvature in the vertical edge direction is much larger than that along the edge direction. The curvature ratio in the two directions can be used to remove the unstable edge response point (Pal and Maiti, 2018). Finding the principal curvature requires solving the eigenvalues of 2 × 2 Hessian matrix H at the candidate eigenvalues, which are:

$$H = \begin{bmatrix} D_{xx} & D_{xy} \\ D_{xy} & D_{yy} \end{bmatrix} \tag{19}$$

In Equation (19), D_{xy} represents the characteristic value of row y and column y.

Since the principal curvature of function $D(X)$ is directly proportional to the eigenvalue of matrix H, the ratio of curvature can be calculated by the ratio between eigenvalues. The ratio is taken as the judgment standard of edge response point removal (Qi et al., 2018). If the ratio of principal curvature is greater than the threshold $T\gamma$, the candidate point is removed.

2.2.3 Feature Point Orientation

In order to enable the feature points to have rotation invariance, we need to assign a main direction to each feature point, which can be constructed by using the gradient amplitude and direction distribution characteristics of each pixel in the neighborhood of the point. For image $L(x, y)$ at scale σ, gradient amplitude $m(x, y)$ and direction $\phi(x, y)$ are calculated by pixel difference:

$$(x, y) = \sqrt{L(x+1, y) - L(x-1, y)^2 + (L(x, y+1) - L(x, y-1))^2} \tag{20}$$

$$\phi(x, y) = \tan^{-1}\frac{L(x-1, y) - L(x, y-1)}{L(x+1, y) - L(x-1, y)} \tag{21}$$

In the actual calculation, the direction and gradient of the pixels in the neighborhood window of the feature points are counted to generate the gradient histogram. The histogram is established with r° as the interval, and there are $\frac{r}{360}$ columns in total. According to the direction $\phi(x, y)$ of each pixel, the gradient $m(x, y)$ is added to the corresponding direction column of the pixel, and the peak position in the gradient histogram is the main direction O_x of the feature point.

2.2.4 Feature Point Descriptor Generation

In order to achieve the subsequent matching, we must construct the feature space for each feature point, and require the feature space to describe the feature points as fully as possible, so as to achieve the similarity between points of the same name and the difference between points of different names, and to maximize the probability of correctly matching the feature points. To ensure the rotation invariance, the coordinate axis direction of the neighborhood is rotated to the main direction O_x of the current feature point X. Taking the feature point as the center, an 8 × 8 pixel window is selected, and the gradient value and direction of pixels

Table 2 Types of targets included in the experimental images.

No.	Target Category	Type
1	Bird's nest	Bird's nest
2	Insulator	Suspension insulator, rod insulator, etc.
3	Tower	Drum Tower, wine glass tower, dry word tower, etc.

are random. Then, eight gradient direction values of each 4×4 neighborhood block are accumulated to form a gradient direction histogram, which is called a seed point. In practical calculation, it is suggested to use 16 seed points of 4×4 to describe, that is, to finally form the feature description vector V_x with $4 \times 4 \times 8 = 128$ dimensions. This method enhances the denoising ability of the algorithm (Zhang et al., 2018).

2.3 Realization of Target Detection of Aerial Image in Power Grid Inspection

Based on the transfer learning algorithm, the detection of a target in aerial images in a power grid inspection is realized, and the algorithm is completed. The main steps of the algorithm are as follows:

(1) For reference image I, the skew parameters are obtained by transfer learning algorithm, and the skew changes caused by latitude angle are simulated. It is equivalent to the transfer learning subsampling in the x-direction. Before sampling, it needs to apply smooth filtering processing, that is to use the Gauss kernel with the standard deviation of Equation (22) for convolution, so as to ensure that there is only a small aliasing error.

$$P = c\sqrt{t^2 - 1} \tag{22}$$

In Equation (22), c stands for constant, t stands for skew parameter and P stands for standard deviation.

(2) The skew parameter and the longitude angle parameter φ are sampled according to certain rules. When the latitude angle ϑ increases according to the fixed angle interval, the image deformation will become larger and larger. Therefore, the sampling density of the latitude parameter should increase with the increase of ϑ. The parameter t should be sampled according to the equal ratio sequence, and the longitude parameter φ should be sampled according to the equal difference sequence related to the latitude parameter t.

(3) The sampling values of the obtained parameters t and φ are substituted into the following equation:

$$\begin{cases} I_k(t_{k1}, \varphi_{k2}) = \begin{bmatrix} \cos\varphi_{k2} & -\sin\varphi_{k2} \\ \sin\varphi_{ks} & \cos\varphi_{k2} \end{bmatrix} \begin{bmatrix} t_{k1} & 0 \\ 0 & 1 \end{bmatrix} \\ k = 1, \ldots, m \times n \end{cases} \tag{23}$$

In Equation (23), t_{k1} represents the sequence of equal ratio in step (2), as shown in Equation (24); φ_{k2} represents the sequence of equal difference in step (2), as shown in Equation (25); I_k represents the analog image of reference image I.

$$\begin{cases} t_{k1} = 1, u, u^2, \ldots, u^m \\ k1 = 0, 1, \ldots, m \end{cases} \tag{24}$$

In Equation (24), m represents constant, u represents the proportional sampling parameter and $u > 1$.

$$\begin{cases} \varphi_{k2} = 0, \frac{v}{t}, \ldots, n\frac{v}{t} \\ k_2 = 0, 1, \ldots, n \end{cases} \tag{25}$$

In Equation (24), n stands for constant and v stands for isochromatic sampling parameter.

(4) The set of feature points of reference image and a series of simulated image are obtained, and the description vector of each feature point is obtained. The set of feature vectors is established respectively, and these feature vector sets together constitute the total set of feature vectors of reference image.

(5) The set of feature points of the distorted image I' is obtained, and the description vectors of each feature point are obtained to establish the set of feature vectors of the distorted image I'.

(6) The two feature vector sets are matched to detect the target in aerial images in the power grid inspection.

3. EXPERIMENTAL STUDY

3.1 Experiment Process

The target detection algorithm for aerial images in power grid inspection based on transfer learning is verified by experiments. The aerial inspection image of UAV is selected as the experimental image, the size of which is 352 * 288 pixels. Most of the images contain complex scenes that include a tower, a large number of transmission lines with insulator strings, some ground with color characteristics similar to the insulator, etc. The target types included in the experimental images are shown in Table 2.

Thirty images were used for the experiments, divided into three groups. Each group's detection target corresponds to the serial number of the target type. The first group of experimental aerial images for the power grid inspection are shown in Figure 3.

The second group of experimental aerial images for the power grid inspection are shown in Figure 4.

Figure 3 The first group of experimental aerial images for power grid inspection.

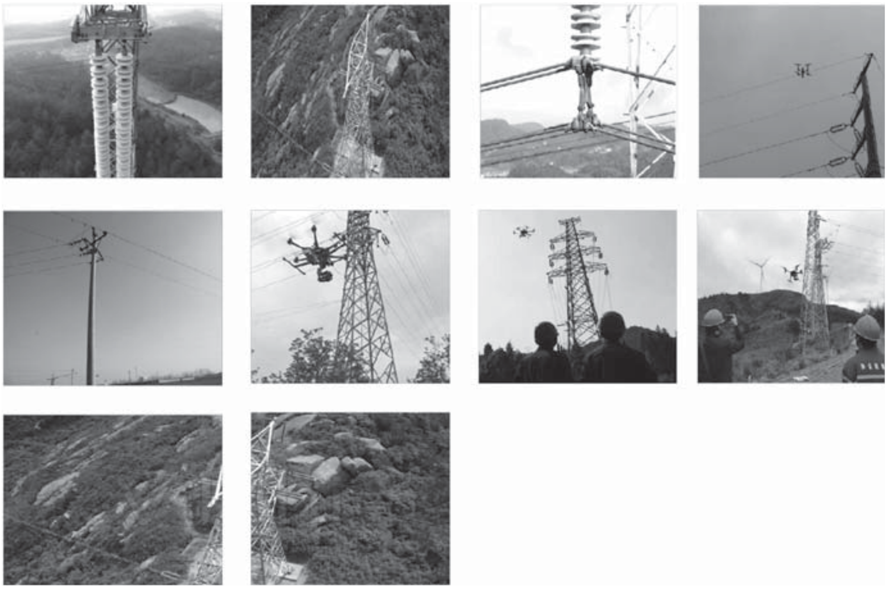

Figure 4 The second group of experimental aerial images for power grid inspection.

The third group of experimental aerial images for the power grid inspection are shown in Figure 5.

The target detection algorithm based on transfer learning is used to detect the target of these 30 aerial images, and the target coincidence rate is 29.56%–49.56%. The recall data in the target compliance rate range is used as the experimental data. The equation for the recall rate is:

$$recall = \frac{A}{A+C} \tag{26}$$

In Equation (26), *recall* stands for recall rate; *recall* stands for the correctly identified target; $A+C$ stands for the number of targets in the test set, as shown in Figure 6.

In order to obtain more than a single result from this experiment, the original two kinds of target detection algorithms for aerial images in power grid inspection are used for comparison; they are the algorithm based on the ratio operator and the genetic algorithm. The recall data yielded by the two algorithms are compared with those obtained with the algorithm proposed in this paper.

3.2 Experimental Results

In the target coincidence rate range of 29.56%–39.56% of the image, the recall rate comparison results of the first group of experimental images using the target detection algorithm based on transfer learning, ratio operator and genetic algorithm are shown in Table 3.

The comparison results for the recall rate for the second group of experimental images are shown in Table 4.

The comparison results for the recall rate of the third group of experimental images are shown in Table 5.

Figure 5 The third group of experimental aerial images for power grid inspection.

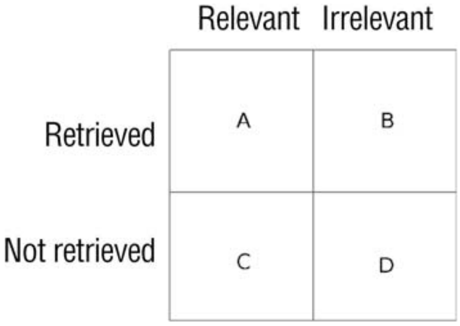

Figure 6 Schematic diagram of recall rate.

Table 3 Comparison test results for the recall rate for the first group of experimental images in the target coincidence rate range of 29.56%–39.56% of image.

		Recall Rate (%)		
Experimental Image Group	**Serial Number of Experimental Image**	**Algorithm based on transfer learning**	**Algorithm based on Ratio operator**	**Algorithm based on genetic algorithm**
First	1	16.3254	23.3697	25.3258
	2	15.3247	21.0258	24.3658
	3	10.2015	29.3254	29.3654
	4	10.0201	24.2015	19.6582
	5	9.3625	29.3247	35.9862
	6	8.3258	15.3369	21.2045
	7	7.3258	19.3258	20.0152
	8	4.2015	18.3256	17.1544
	9	8.3024	16.3258	18.3628
	10	7.0215	14.9696	22.3688
Mean value		9.64112	21.15308	23.164589

According to the experimental results above, for the range of 29.56%–39.56%, the recall rate of the algorithm based on transfer learning is always lower than that based on the ratio operator and genetic algorithm.

In the target coincidence rate range of 39.56%–49.56% of the image, the experimental results of the recall rate for the third group of experimental images based on the transfer learning are compared with those of the other two algorithms are shown in Table 6.

In the target coincidence rate range of 39.56%–49.56% of the image, the experimental results of the recall rate for the third group of experimental images based on the transfer

Table 4 Comparison test results for the recall rate of the second group of experimental images.

		Recall Rate (%)		
Experimental Image Group	**Serial Number of Experimental Image**	**Algorithm based on transfer learning**	**Algorithm based on Ratio operator**	**Algorithm based on genetic algorithm**
	1	9.3647	19.3627	21.0247
	2	3.3694	20.0201	20.0148
	3	5.2022	18.3007	19.3366
	4	10.2581	25.3011	18.2014
	5	9.3821	23.3689	19.3663
Second	6	2.0358	10.2058	15.2018
	7	9.3655	11.3288	14.2018
	8	4.3055	17.2166	26.3014
	9	8.0124	19.3857	19.3302
	10	7.0917	13.9616	21.3668
Mean value		6.83874	17.8452	19.43458

Table 5 Comparison test results for recall rate of the third group of experimental images.

		Recall Rate (%)		
Experimental Image Group	**Serial Number of Experimental Image**	**Algorithm based on transfer learning**	**Algorithm based on Ratio operator**	**Algorithm based on genetic algorithm**
	1	8.2204	18.3387	25.0249
	2	4.3695	22.0201	22.0054
	3	3.6951	17.2177	14.3045
	4	9.3101	20.3214	12.0128
	5	8.3201	20.3021	11.3053
Third	6	9.3014	19.2056	19.0418
	7	2.3025	13.3228	19.2098
	8	2.3925	12.2156	22.3964
	9	6.0022	17.3801	18.3369
	10	5.0187	10.9021	20.3087
Mean value		5.89325	17.12262	18.39465

Table 6 Recall rate comparison test results of the first group of experimental images.

		Recall rate (%)		
Experimental Image Group	**Serial Number of Experimental Image**	**Algorithm based on transfer learning**	**Algorithm based on Ratio operator**	**Algorithm based on genetic algorithm**
	1	2.6947	20.0111	22.0210
	2	5.3004	19.3320	20.3021
	3	1.0258	16.3028	21.0214
	4	3.3692	19.3021	18.3225
	5	4.6358	25.0214	24.2014
First	6	8.3201	20.0001	20.6978
	7	6.3048	23.3021	27.0102
	8	3.2018	19.3216	13.2504
	9	9.2585	18.3688	11.3012
	10	4.2015	10.9366	12.0588
Mean value		4.83126	19.18986	19.01868

Table 7 Recall rate comparison test results for the second group of experimental images.

		Recall Rate (%)		
Experimental Image Group	**Serial Number of Experimental Image**	**Algorithm based on transfer learning**	**Algorithm based on Ratio operator**	**Algorithm based on genetic algorithm**
Second	1	2.3369	11.3607	22.0367
	2	1.3058	10.0381	24.0147
	3	5.0252	17.0147	21.0002
	4	12.2071	22.0171	17.2194
	5	8.3301	20.3691	15.3600
	6	3.1248	10.2086	16.2880
	7	6.3285	14.3247	10.2318
	8	3.3595	13.2148	25.3018
	9	4.0192	15.0107	13.7902
	10	6.0367	11.9046	20.3614
Mean value		5.20738	14.54631	18.56042

Table 8 Comparison test results for recall rate of the third group of experimental images.

		Recall Rate (%)		
Experimental Image Group	**Serial Number of Experimental Image**	**Algorithm based on transfer learning**	**Algorithm based on Ratio operator**	**Algorithm based on genetic algorithm**
Third	1	2.0214	16.6667	20.0019
	2	4.0893	20.0285	20.0078
	3	5.6900	11.0007	16.3025
	4	8.3761	21.0004	11.0198
	5	7.3207	20.0587	16.3269
	6	8.3128	17.2766	14.0302
	7	5.3193	14.3028	18.2021
	8	1.3396	10.2126	21.0896
	9	5.0004	18.3011	17.3309
	10	5.0188	12.9008	27.3697
Mean value		5.24884	16.17489	18.16814

learning are compared with those of the other two algorithms are shown in Table 7.

In the target coincidence rate range of 39.56%–49.56% of the image, the experimental results of the recall rate for the third group of experimental images based on the transfer learning are compared with those of the other two algorithms are shown in Table 8.

According to the experimental results above, in the target coincidence rate range of 39.56%–49.56% of the image, the recall rate of the image target detection algorithm based on transfer learning is always lower than that based on the ratio operator and genetic algorithm.

4. CONCLUSIONS

The target detection algorithm based on transfer learning can be applied to the automatic inspection of future railway transmission lines and the entire national power grid transmission lines, giving it a broad range of applications.

REFERENCES

1. Chowdhary A., Kumar A. 2019. Study of Web Page Ranking Algorithms: A Review. *Acta Informatica Malaysia, 3*(2), 01–04.
2. D'Aniello, C., Pisconti, S., Facchini, S., et al. 2018, Long noncoding RNA GIHCG is a potential diagnostic and prognostic biomarker and therapeutic target for renal cell carcinoma. *European review for medical and pharmacological sciences, 22*(5), 1169–1170.
3. Gian S.H., Kasim S., Hassan R., Zakaria Z., Mahdin H., Ramli A.A., Md Fudzee M.F., Salamat M.A. 2019. Online Activity Duration Management System for Manufacturing Company. *Acta Electronica Malaysia, 3*(2), 01–08.
4. Gao G.B., Gu J.Q. 2018. Research on The Training Mode Of E-Business Professionals Under the Background of New Retailing Model. *Information Management and Computer Science, 1*(2), 21–23.
5. He, J., Yu, L., Wang, C.M., et al. 2018, MiR-1275 promotes non-small cell lung cancer cell proliferation and metastasis by regulating LZTS3 expression. *European Review for Medical and Pharmacological Sciences, 22*(9), 2680–2687.

6. Hou, X.S., Han, C.Q., Zhang, W. 2018, MiR-1182 inhibited metastasis and proliferation of ovarian cancer by targeting hTERT. *European Review for Medical and Pharmacological Sciences, 22*(6), 1622–1628.
7. Jiang, H., Qu, P., Wang, J.W., et al. 2018, Effect of NF-κB inhibitor on Toll-like receptor 4 expression in left ventricular myocardium in two-kidney-one-clip hypertensive rats. *European Review for Medical and Pharmacological Sciences, 22*(10), 3224–3233.
8. Jonsson, N.N. 2018, Molecular biology of amitraz resistance in cattle ticks of the genus i Rhipicephalus i. *Frontiers in Bioscience, 23*(2), 796–810.
9. Liu, D.K., Wei, Y.J., Guo, Y., et al. 2018, MiRNA-93 functions as an oncogene in glioma by directly targeting RBL2. *European Review for Medical and Pharmacological Sciences, 22*(8), 2343–2350.
10. Lou, L., Yu, Z., Wang, Y., et al. 2018, C-src inhibitor selectively inhibits triple-negative breast cancer overexpressed Vimentin in vitro and in vivo. *Cancer Science, 109*(5), 1648–1659.
11. Luo, Y., Ouyang, J., Zhou, D., et al. 2018, Long noncoding RNA GAPLINC promotes cells migration and invasion in colorectal cancer cell by regulating miR-34a/c-MET signal pathway. *Digestive Diseases and Sciences, 63*(4), 1–10.
12. Maria, S. 2018, Genetic organization of i Streptococcus salivarius i 24SMBc i blp i -like bacteriocin locus. *Frontiers in Bioscience*, 10(1), 238–247.
13. Milliat, F., Agnés, F. 2018, The roles of mast cells in radiation-induced damage are still an enigma. *Médecine/Sciences, 34*(2), 145–154.
14. Nagaraj, K., Lapkina Gendler, L., Sarfstein, R., et al. 2018, Identification of thioredoxin-interacting protein (TXNIP) as a downstream target for IGF1 action. *Proceedings of the National Academy of Sciences, 115*(5), 1045–1050.
15. Pal, D., Maiti, S.K. 2018, Seasonal variation of heavy metals in water, sediment, and highly consumed cultured fish (Labeo rohita and Labeo bata) and potential health risk assessment in aquaculture pond of the coal city, Dhanbad (India). *Environmental Science and Pollution Research, 25*(13), 12464–12480.
16. Pavela, R. 2018, Essential oils from Foeniculum vulgare Miller as a safe environmental insecticide against the aphid Myzus persicae Sulzer. *Environmental Science and Pollution Research, 25*(2), 1–7.
17. Qi, X.D., Xu, S.Y., Song, Y. 2018, Prognostic value of long non-coding RNA HOST2 expression and its tumor-promotive function in human osteosarcoma. *European Review for Medical and Pharmacological Sciences, 22*(4), 921–927.
18. Sophie, V.S. 2018, The future of telomere length in personalized medicine. *Frontiers in Bioscience, 23*(9), 1628–1654.
19. Wang, H., Liu, L., Liu, X., et al. 2018, Correlation between miRNAs and target genes in response to Campylobacter jejuni inoculation in chicken. *Poultry Science, 97*(2), 485–493.
20. Zhang, J., Xing, H.,Lu, Y. 2018, Translating molecular detections into a simple temperature test using a target-responsive smart thermometer. *Chemical Science, 9*(16), 3906–3910.
21. Zhang, R., Xu, J., Zhao, J., et al. 2018, Silencing of hsa-circ-0007534 suppresses proliferation and induces apoptosis in colorectal cancer cells. *European Review for Medical and Pharmacological Sciences, 22*(1), 118–126.
22. Zou, Y., Huang, S., Liao, Y., et al. 2018, Isotopic graphene-isolated-Au-nanocrystals with cellular Raman-silent signals for cancer cell pattern recognition. *Chemical Science, 9*(10), 2842–2849.